Nanoscale

Accepted Manuscript

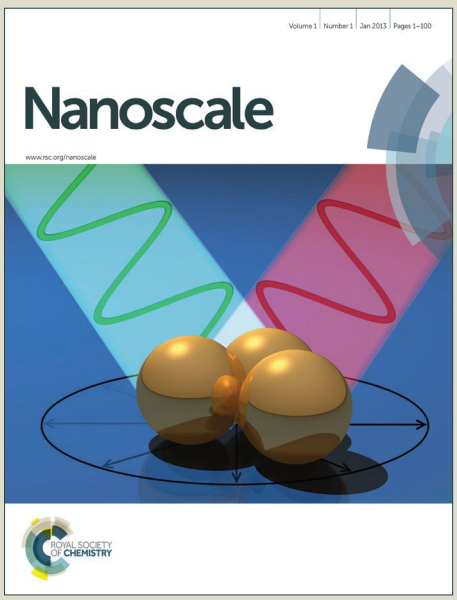

ROYAL SOCIETY OF CHEMISTRY

www.rsc.org/nanoscale

Combined Flame and Solution Synthesis of Nanoscale Tungsten-Oxide and Zinc/Tin-Oxide Heterostructures

Zhizhong Dong[1], Di Huo[2,3], Bernard Kear[2], and Stephen D. Tse[1*]

[1]*Department of Mechanical and Aerospace Engineering, Rutgers University, Piscataway, New Jersey 08854*

[2]*Department of Materials Science and Engineering, Rutgers University, Piscataway, New Jersey 08854*

[3]*Key Laboratory of Anisotropy and Texture of Materials (Ministry of Education), Northeastern University, Shenyang 110004, China*

**corresponding author, email: sdytse@rci.rutgers.edu*

Abstract

Heterostructures of tungsten-oxide nanowires decorated with zinc/tin-oxide nanostructures are synthesized *via* a combined flame and solution synthesis approach. Vertically well-aligned tungsten-oxide nanowires are grown on the tungsten substrate *via* flame synthesis method. Here, tetragonal $WO_{2.9}$ nanowires (diameters of 20-50 nm, lengths > 10 μm, and coverage density of 10^9-10^{10} cm^{-2}) are produced by the vapor-solid mechanism at 1720 K. Various kinds of Zn/Sn-oxide nanostructures are grown or deposited on the $WO_{2.9}$ nanowires by adjusting the Sn^{2+}:Zn^{2+} molar ratio in an aqueous ethylenediamine solution at 65 °C. With $WO_{2.9}$ nanowires serving as the base structures, sequential growth or deposition on them of hexagonal ZnO nanoplates, Zn_2SnO_4 nanocubes, and SnO_2 nanoparticles are attained for Sn^{2+}:Zn^{2+} ratios of 0:1, 1:10, and 10:1, respectively, along with different saturation conditions. High-resolution transmission electron microscopy of the interfaces at the nanoheterojunctions shows abrupt interfaces for ZnO/$WO_{2.9}$ and Zn_2SnO_4/$WO_{2.9}$, despite lattice mismatches of >20%.

Keywords

Heterostructure, Tungsten oxide, Zinc oxide, Tin oxide, Zinc tin oxide

Introduction

One-dimensional (1-D)-based heterostructured nanomaterials have attracted significant attention due to their enhanced physical and chemical properties, allowing them to be employed in electronic, photonic, and sensing devices[1,2]. Accordingly, various approaches have been used to obtain the desired 1-D-based nanomaterials (*e.g.* coaxial nanowires[3], segmented nanowires[4], and hierarchical nanowires[5]). Either single or combined methods can be utilized to produce 1-D-based nanomaterials with multiple components and complex structures.

By using a single method, generally gas-phase techniques, such as chemical vapor deposition (CVD)[6], molecular beam epitaxy (MBE)[7], and pulsed-laser deposition (PLD)[8], have been used to synthesize nanoheterostructures by sequentially alternating the supply of different precursors. For example, with Au nanoparticles as catalyst (~140 nm diameter), Zakharov *et al.*[7] produced alternating Si/Ge segmented nanowires (60-180 nm diameter, 200 nm length) on Si wafer (<111> oriented) at 545 °C, using MBE by alternating Si and Ge vapor sources through two different electron-beam guns, for 2 hours. Gudiksen *et al.*[8] grew GaAs/GaP (20 nm diameter, 3 μm length) nanowires, also with Au nanoparticles (~20 nm diameter) as catalyst, by using PLD with the substrate at ~700 °C, by ablating solid GaAs and GaP targets one after the other to supply the vapor-phase precursors.

More commonly, multiple synthesis methods are combined to fabricate 1-D-based heterostructured nanomaterials. CVD, PLD, and MBE are often used as gas-phase methods to fabricate a given composition of base-structure nanowires/nanotubes through the vapor-liquid-solid (VLS) or vapor-solid (VS) route. Then, depending on the type of precursor and its characteristics (*e.g.* volatility), another method, which can be vapor-phase or wet chemistry, builds upon the previous material to obtain the final desired hetero-nanomaterial. Combinations

such as CVD-thermal evaporation (*e.g.* NiSi/Si segmented nanowires[9]), PLD-CVD (*e.g.* Si/SiGe nanowires[10]), CVD-MBE (*e.g.* GaAs/Si hierarchical nanowires[11]), and PLD-solution (*e.g.* Se/Ag_2Se core/shell nanowires[12]) have been investigated.

Nevertheless, for gas-phase methods producing the base-structure nanowires, the growth rates and yields are often low, along with the complex processing requirements, involving catalysts[9], pretreatment[10], long durations[11], and vacuum systems[12]. The growth of nanowires over large areas remains especially challenging. However, flame synthesis has demonstrated a history of scalability and high-volume production, along with economy due to its inherent source of heating. It has shown an excellent capability to rapidly produce dense arrays of many types of metal-oxide (e.g. ZnO nanowires[13], Fe_2O_3 nanowires[14], WO_3 nanorods[15], and MoO_3 nanobelts[16]) and carbon (*e.g.* carbon nanotubes[17–19], graphene[20–22]) nanostructures, which can be readily employed as the starting building blocks for the fabrication of heterostructured nanomaterials. Moreover, synthesis can be accomplished without any pretreatment or catalysts, in open environments, over large areas, and in short durations[13–17].

Accommodating lattice mismatches between different nanoscale materials can provide promising physical and chemical performances, which usually cannot be obtained from their bulk counterparts[1,23]. Wu *et al.*[9] fabricated NiSi/Si segmented nanowires with spatially abrupt and electronically well-defined interface between NiSi (growth direction of [221]) and Si (growth direction of [112]), demonstrating high hole-mobility of 325 cm^2Vs at room temperature as a 1-D nanoscale field-effect transistor (FET). Milliron *et al.*[23] epitaxially grew CdTe on the tips of CdS nanorods, with stacking-fault-free continuous growth of linear junctions despite large lattice mismatch (11%) between CdTe and CdS. Typically, multiple synthesis methods/steps, *e.g.* involving vapor-liquid-solid[10], vapor-solid[24], solution-liquid-solid (SLS)[25], and solution-solid

(SS)[26] routes, are utilized to produce heterostructured nanomaterials. For example, using a two-method/step process involving thermal evaporation and chemical bath deposition, Kim *et al.*[27] decorated WO_3 nanowhiskers (diameters of 80 nm-1 μm) with CdS nanoparticles (diameters of 20-50 nm), which possessed enhanced photocatalytic efficiencies.

Here, we report the unique decoration of Zn/Sn-oxide nanostructures (produced by solution synthesis) on vertically well-aligned tungsten-oxide nanowires (produced by flame synthesis). Applying solution synthesis in the second step affords several advantages[28]. For dilute solutions, lower growth rates allow for improved thickness control in epitaxial situations. Concurrently, lower growth temperatures provide for improved structural perfection and stoichiometry, while also reducing the effects of thermal expansion differences between the base nanostructure and the secondarily-grown material. The degree of saturation can be controlled, ranging from epitaxially-grown material to spontaneously-nucleated crystallites (that can then deposit on the nanowires). In this work, hexagonal ZnO nanoplates, Zn_2SnO_4 nanocubes, and SnO_2 nanoparticles are grown or deposited on $WO_{2.9}$ nanowires, where the composition and morphology of the added nanostructures are controlled by the ratio of tin to zinc ions in the aqueous solution in the presence of the $WO_{2.9}$ nanowires.

Recently, the enhanced physical and chemical properties of tungsten-oxide nanomaterials (*e.g.* WO_3 nanoparticles and nanowires) make them promising candidates for various applications, such as gas sensors (*e.g.* for NO[29], NO_2[30], and NH_3[31]), electrochromic devices[32], and photocatalysts[33]. These tungsten-oxide nanomaterials can then be utilized as essential building blocks to fabricate multi-component and heterostructured nanomaterials with specific improved properties, including W/WO_3 (field emission)[24], CdS/WO_3 (photocatalysis)[27], $SnO_2/W_{18}O_{49}$ (chemical sensor)[34], TiO_2/WO_3 (energy conversion)[35], ZnO/WO_3 (gas sensing)[36],

and WO_3/$BiVO_4$ (photoelectrochemical water splitting)[37]. As such, in this work, we combine the benefits of gas-phase and solution syntheses to produce compositionally-relevant nanostructures with unique heterojunctions.

A schematic diagram of the approach is given in **Figure 1**. In the first step, a counter-flow diffusion flame is utilized to synthesize vertically well-aligned $WO_{2.9}$ nanowires grown directly from the surface of a tungsten wire substrate[38]. The synthesis method is robust in that the combustion process inherently provides for *i*) an elevated enthalpy source to vaporize metal/metal-oxide substrate species, *ii*) the gas-phase chemical species *e.g.* oxygen, water vapor, carbon dioxide, and hydrogen to produce the requisite oxide, and *iii*) a favorable temperature gradient for growth of the nanowires. Using the quasi-one-dimensional diffusion flame, many local growth conditions (*i.e.* temperature, gas-phase species concentrations) as a function of axial position can be scanned in a single flame, determining optimum "universal" growth conditions that can be translated to other flame configurations (*e.g.* stagnation point flow) that are better suited for synthesis over large areas. Parenthetically, carbon nanostructures (i.e. carbon nanotubes and graphene) can also be readily produced in such counterflow[18, 39] and stagnation flames[22, 40], and would be of interest in serving as base structures for secondary nanomaterial growth. In the second step, solution synthesis, using zinc nitrate hexahydrate and tin chloride dehydrate as precursors in aqueous ethylenediamine solutions, is utilized to grow different compositions and morphologies of nanomaterials (ZnO, Zn_2SnO_4, and SnO_2) on the scaffold $WO_{2.9}$ nanowires, as shown in **Figure 1**, forming heterostructured nanomaterials. As shown in **Table 1**, solutions with different amounts of precursor compositions and concentrations are used for the corresponding cases (Case 1-9). The experimental process is detailed in the Methods Section.

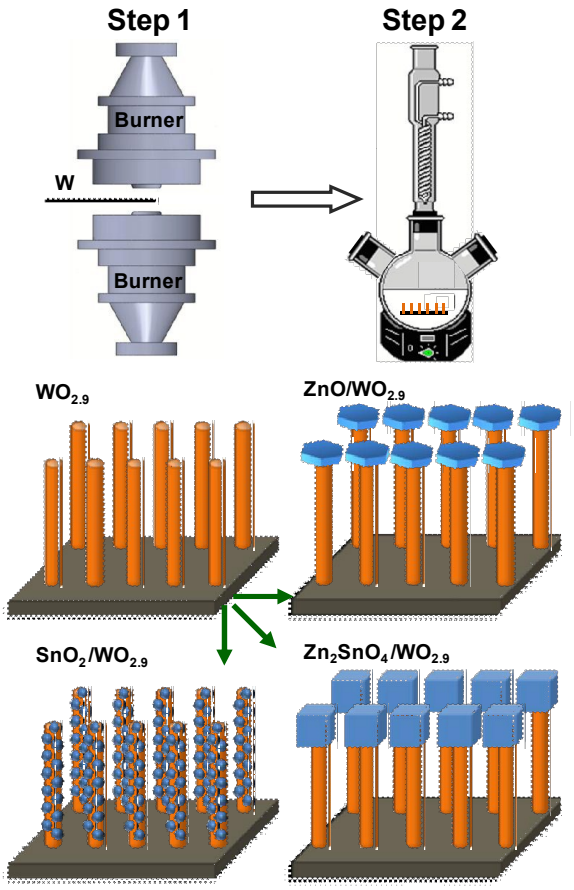

Figure 1. Schematic diagram of the two-step experimental setup. In the 1st step, $WO_{2.9}$ nanowires are produced *via* the flame synthesis method. In the 2nd step, the growth of secondary components is done by the solution method.

Table 1. Composition of solution (2nd step) for different cases.

Case	$C_2H_4(NH_2)_2$ /mM	$Zn(NO_3)_2{\cdot}6H_2O$ /mM	$SnCl_2{\cdot}2H_2O$ /mM
1	5	5	0
2	5	5	0.5
3	5	4	1
4	5	3	2
5	5	2	3
6	5	1	4
7	5	0.5	5
8	5	0	5
9	0.5	0	0.5

Results and Discussion

$WO_{2.9}$ Nanowires Array. As shown in the FESEM image, **Figure 2a**, the $WO_{2.9}$ nanowires (diameters of 20-50 nm and lengths>10 μm) grow directly from the surface of the tungsten substrate with high coverage density of 10^9-10^{10} cm^{-2}, for a 10 min growth time indicating the high growth rate of >1 μm/min. Moreover, **Figure 2b** reveals the vertical and well-aligned growth of $WO_{2.9}$ nanowires without any catalysts, which is governed by the VS mechanism[15,38]. Here, the combustion process inherently provides an elevated enthalpy/temperature source to rapidly produce W/O related species which come from the redox reactions between W and the gas-phase species such as O_2, CO_2 and H_2O[13,38]. **Figure 2c** shows a low-magnification TEM image of a single $WO_{2.9}$ nanowire revealing its well-defined wire shape. The SAED pattern (inset of **Figure 2c**) confirms it as tetragonal $WO_{2.9}$ (PDF #18-1417). **Figure 2d** presents the side-view HRTEM image of a single as-produced $WO_{2.9}$ nanowire, showing its dislocation-free and single-crystal feature, with a lattice spacing of 3.78 Å and [110] growth direction.

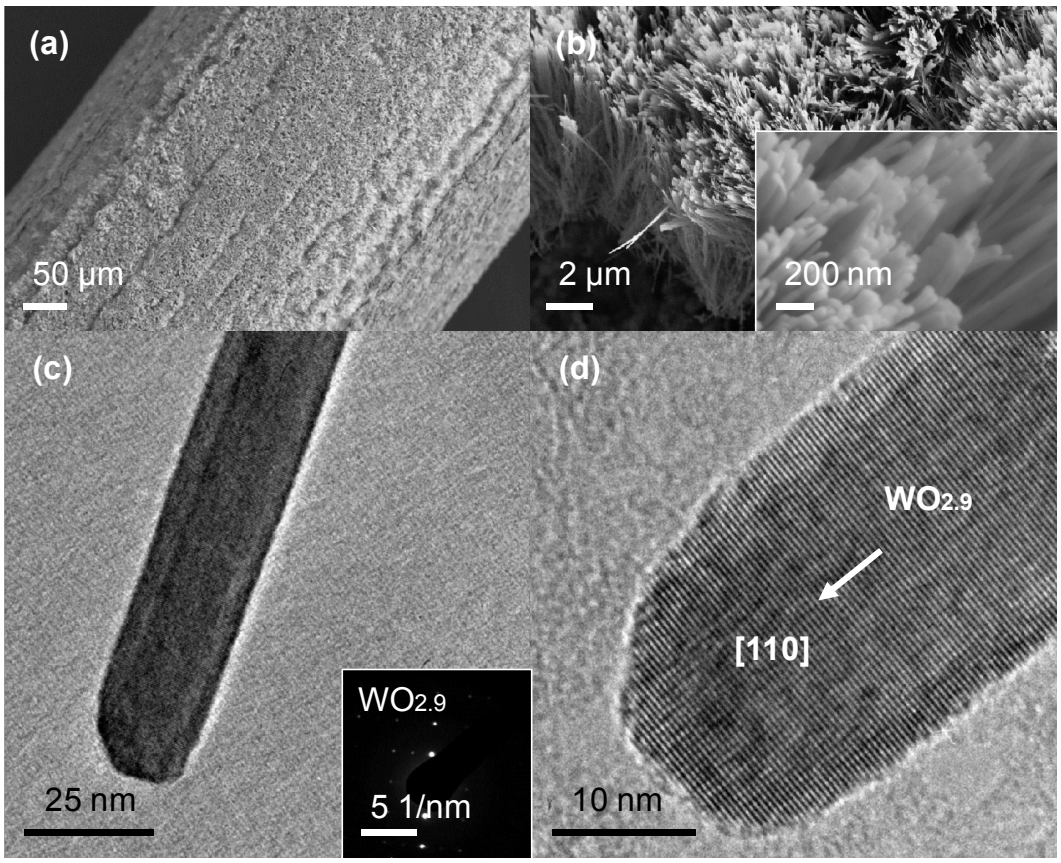

Figure 2. (a) Top-view low-magnification FESEM image of flame-synthesized $WO_{2.9}$ nanowires array with high density of yield. (b) Side-view low-magnification FESEM image of $WO_{2.9}$ nanowires showing the vertical growth feature; the inset shows the side-view high-magnification FESEM image of the nanowires. (c) Top-view low-magnification TEM image of a single $WO_{2.9}$ nanowire; inset shows the corresponding SAED pattern. (d) Side-view HRTEM image of a single as-synthesized $WO_{2.9}$ nanowire with [110] growth direction.

ZnO on the Tips of $WO_{2.9}$ Nanowires (Case 1). As shown in **Figure 3a**, abundant heterostructured nanomaterials are found on the surface of the tungsten substrate. Nearly all tips of $WO_{2.9}$ nanowires are capped with hexagonal ZnO nanoplates. During the solution synthesis process, ethylenediamine gradually decomposes around 65 °C, continuously providing ammonia which then forms ammonium hydroxide and complex intermediates with zinc ions[41]. Subsequently, the dehydration of these intermediates leads to the formation of desired zinc

oxides[41–46]. For the formation of ZnO, we hypothesize that the global chemical reactions involved are:[41–46]

$$C_2H_8N_2 + 2H_2O \rightarrow 2NH_3 + C_2H_6O_2 \quad (1)$$

$$NH_3 + 2H_2O \rightarrow NH_4^+ + OH^- \quad (2)$$

$$2OH^- + Zn^{2+} \rightarrow ZnO(s) + H_2O \quad (3)$$

Briefly, the desired amount of OH^- ions is produced through Reactions 1 and 2 at 65 °C, followed by reactions with zinc ions in the solution. After the dehydration of Zn/O-related intermediates, nucleation and growth of ZnO nanoplates take place at the tips of the $WO_{2.9}$ nanowires as the preferred sites. Hou *et al.*[47] observed the growth of vertically aligned ZnO nanowires (~80 nm diameter), *via* the Au-assisted VLS mechanism, at the nodes of a 2-D network of ZnO nanowalls (~80 nm thickness), where such nodes are believed to be the most thermodynamically active nucleation sites for the saturation and precipitation of Zn/O related monomers. Here, the tips of $WO_{2.9}$ nanowires most likely play a similar role as the favorable heterogeneous nucleation sites or "kinks" for the formation of ZnO nanoplates, in these end-to-end type ZnO/$WO_{2.9}$ heteronanostructures[48–51]. Subsequently, the continued "radial" growth, where the velocities of crystal growth in different directions are $V_{<01\bar{1}0>} > V_{<01\bar{1}1>} > V_{<000\bar{1}>} = V_{<0001>}$ according to PBC theory[52] of the initially formed hexagonal ZnO nanoplates may be promoted via the continuous diffusion and adsorption of Zn/O related monomers. As proposed by others[53-55], the fundamental growth units of the ZnO nanocrystal are likely to be the complex $Zn(OH)_4^{2-}$, where the stacking assembly of the ZnO nanocrystals arise from the interaction between the surface hydroxides of the growing crystals and the hydroxide ligands of the zinc complexes.

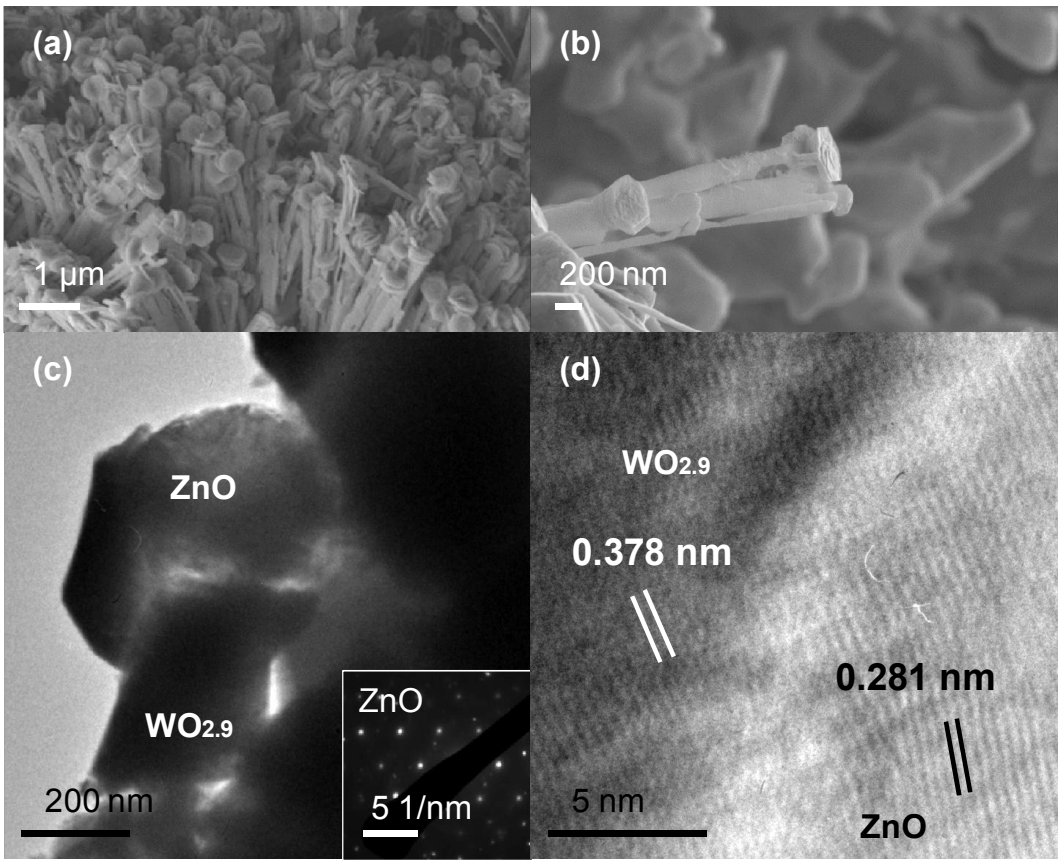

Figure 3. (a) Side-view low-magnification FESEM image of as-synthesized ZnO/$WO_{2.9}$ heterojunction nanowires. (b) Side-view high-magnification FESEM image of the ZnO/$WO_{2.9}$ heterojunction nanowires. (c) Low-magnification TEM image of a single ZnO/$WO_{2.9}$ heterojunction; inset shows the SAED pattern from ZnO. (d) HRTEM image of the interface between ZnO and $WO_{2.9}$.

Figure 3b shows that the ZnO nanoplates have thicknesses of 40–60 nm and lateral widths of 170–200 nm. Also, the diameters of $WO_{2.9}$ nanowires increase to 150–200 nm after the solution synthesis process, which is most likely caused by deposition of Zn/O related species on the surface of the original $WO_{2.9}$ nanowires[5,56]. Similarly, Baek *et al.*[24] found that during their two-step gas phase synthesis of W/WO_3 hierarchical heterojunctions, a film of W coated the surface of WO_3 nanorods (diameters of 200-500 nm), which was followed by further formation of nuclei on the W film for the anisotropic growth of W nanowires (diameters of 20-60 nm). From the SAED pattern of the ZnO nanoplate, inset of **Figure 3c**, the indexed spots with *d*-

spacings of 2.81 Å and 1.60 Å match well with the reflections from the {100} and {110} planes of hexagonal phase ZnO (PDF #97-15-5780), respectively. The HRTEM image, **Figure 3d**, shows the interface between $WO_{2.9}$ and ZnO. Again, the lattice planes from $WO_{2.9}$ have *d*-spacing of 3.78 Å, corresponding to the reflections from the {110} planes of tetragonal $WO_{2.9}$[38]. The lattice planes from ZnO with *d*-spacing of 2.81 Å correspond to the reflections from {100} planes of hexagonal ZnO, consistent with the SAED results. Because of the relatively large lattice mismatch of 25.7% between the planes of $WO_{2.9}$ and ZnO, lattice dislocations can be observed at the interface region. Similar interface structures were found in CdS/CdSe heterojunctions, as reported by Ouyang *et al.*[25]. Slight stacking faults between the planes of CdS {002} and CdSe {002} were due to the alike wurtzite structure with small mismatch of <5%. On the other hand, Shen *et al.*[57] observed high density of defects between the {101} planes (*d*-spacing of 0.21 nm) of Zn and the {001} planes (*d*-spacing of 0.63 nm) of ZnS with very large lattice mismatch of 66.7%. Nonetheless, atomically sharp interfaces of heterojunctions have been successfully fabricated, such as for NiSi/Si[9], CdTe/CdS[23], and Ge/ZnS[57]. As found in the literature[1], atomically abrupt interfaces can readily be obtained between two materials with matched lattice structures. However, it is also possible for two materials with lattice mismatches to form atomically abrupt interfaces or slight defect-containing interfaces at nanoscale in solution synthesis[1,28].

To demonstrate the essential role of the scaffold $WO_{2.9}$ nanowires in producing the morphologies of nanostructures from solution, an experiment is performed using a bare tungsten substrate without the $WO_{2.9}$ nanowires (with the same solution composition and synthesis conditions as for Case 1). After the solution synthesis process, as seen from **Figure 4a**, some (but very few) ZnO nanoparticles precipitate out and deposit on the surface of tungsten substrate.

However, the morphology of these as-obtained ZnO nanoparticles is quite different from that given in Case 1. As indicated by the red arrow in **Figure 4b**, the small ZnO nanoparticles (average length of ~300 nm and thickness of ~100 nm) form larger spherical agglomerates with an average diameter of ~1.5 µm. As such, the presence of the $WO_{2.9}$ nanowires strongly affects the solution crystal growth of the subsequent Zn-based nanostructures and their heterojunction interfaces. Structural defects or kinks on the tip of the nanowire make ideal locations for nucleation, allowing adatoms to attach and grow into new nanocrystals under proper conditions. For example, the screw-dislocation of a surface is believed to be one of the important driving forces for the growth of 1-D nanowires. Moreover, with our flame-synthesized nanowires produced by a ledge-growth mechanism, the tips are especially conducive for further growth.

For gas-phase synthesis, flame-assisted CVD-type synthesis has shown ZnO nanostructures heterogeneously growing from other ZnO nanostructures[13, 58]. Not only do these secondary structures emanate from tips but also along lateral surfaces, where various imperfections can serve as nucleation sites. Thus, depending on the conditions of the solution (i.e. temperature, supersaturation, pH) in our second step, these less "defective" or less "kinky" sites can also nucleate new structures, as will be discussed in the next section.

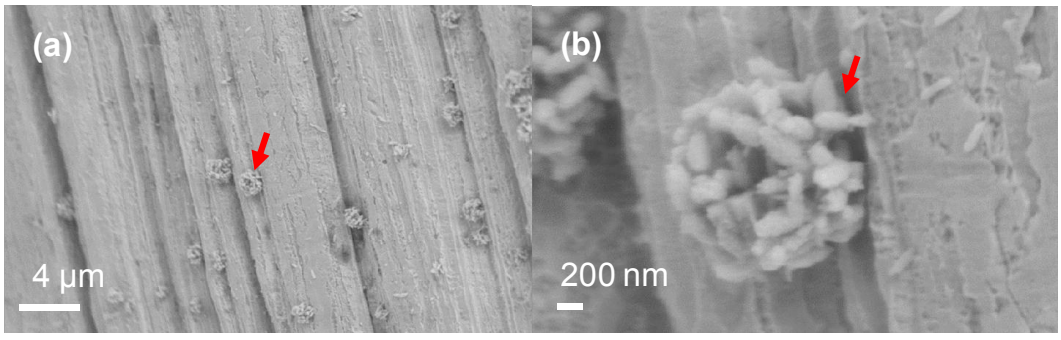

Figure 4. (a) Top-view FESEM image of tungsten substrate after solution synthesis process, showing some ZnO nanoparticles growing on its surface. (b) High-magnification FESEM image of a single ZnO particle with agglomerated structure.

Zn_2SnO_4 on the Tips of $WO_{2.9}$ Nanowires (Cases 2-4). Different amounts of $SnCl_2$ are introduced into the solution corresponding to different Sn:Zn molar ratios (as shown in **Table 1**) to produce spinel compounds of zinc stannate (ZTO, Zn_2SnO_4) in nanocube form. Possible global routes for reaction now include:[59–61]

$$8OH^- + 2Zn^{2+} + Sn^{2+} \rightarrow Zn_2SnO_4(s) + 4H_2O \quad (4)$$

$$4OH^- + Sn^{2+} \rightarrow SnO_2(s) + 2H_2O \quad (5)$$

In other works, various zinc-related spinels have been produced, such as $ZnFe_2O_4$[62], $ZnAl_2O_4$[63], and Zn_2SnO_4[64]. Zn_2SnO_4 is a candidate material for photocatalysts[59,60], Li-ion battery anodes[61], and gas sensors[64]. Here, the Zn_2SnO_4 nanocubes are formed at the tips of the $WO_{2.9}$ nanowires, as shown in **Figure 5,** similar to the previously-presented end-to-end type growth of ZnO/$WO_{2.9}$ heterojunctions of hexagonal ZnO nanostructures on the tips of $WO_{2.9}$ nanowires from Case 1. The Zn_2SnO_4 nanocubes obtained from Cases 2 and 3 have similar sizes of ~200 nm, **Figure 5a**, **5b**, **5c**. However, as shown in **Figure 5d**, the size of the Zn_2SnO_4 nanocubes from Case 4 is ~100 nm, which is much smaller than those for the other cases, despite the same growth duration of 2.5 hours. The size shrinking may be caused by the decreasing of the Zn:Sn molar ratio below a critical value (such as 2), i.e. 10, 4, and 1.5 for cases 2, 3, and 4, respectively, where additionally the concentration of zinc ions decreases from 5 mM to 4 mM to 3mM. TEM image (**Figure 6a**) displays the side-view of a single Zn_2SnO_4/$WO_{2.9}$ heterojunction. As indicated by the red arrow, the $WO_{2.9}$ nanowire was broken during the TEM sample

preparation process, with a short stem remaining, on which a Zn_2SnO_4 nanocube has been epitaxially grown. From the SAED pattern, inset of **Figure 6a**, the indexed spots with *d*-spacings of 5.00 Å and 8.33 Å match well with the reflections from {111} and {100} planes of cubic Zn_2SnO_4 (PDF #97-02-4234), respectively. From HRTEM at the interface, as shown in **Figure 6b**, the *d*-spacing of 3.78 Å corresponds to {110} planes of $WO_{2.9}$; and the *d*-spacing of 5.00 Å corresponds to {111} planes of Zn_2SnO_4, corresponding to a lattice mismatch of 32.3%. This value is larger than the 25.7% for ZnO (100)/$WO_{2.9}$ (110) in Case 1. However, only slight stacking faults are observed at the interface region between Zn_2SnO_4 and $WO_{2.9}$. The results seem to confirm that sharp interfaces at heterojunctions can be formed between different nanomaterials despite large lattice mismatches, which usually cannot be obtained in their bulk counterparts[1,28,57]. We hypothesize that the formation of Zn_2SnO_4/$WO_{2.9}$ heterojunctions is governed by the self-assembly and solution-solid mechanisms. The Zn and Sn related precursors diffuse to the tips of the $WO_{2.9}$ nanowires and nucleate as Zn_2SnO_4 nanostructures. Similar to ZnO construction, Sn complexes are likely involved in the assembly of SnO nanostructures; and both Zn and Sn complexes are likely involved in the growth of Zn-Sn-O compounds. Further crystallization of cube-shaped Zn_2SnO_4 at equal velocities for all faces is most likely promoted under the given saturation conditions. Nevertheless, more investigations are still needed to understand the interface formation mechanisms. The process may be affected by crystal structure, size, and synthesis procedure[1,48,57].

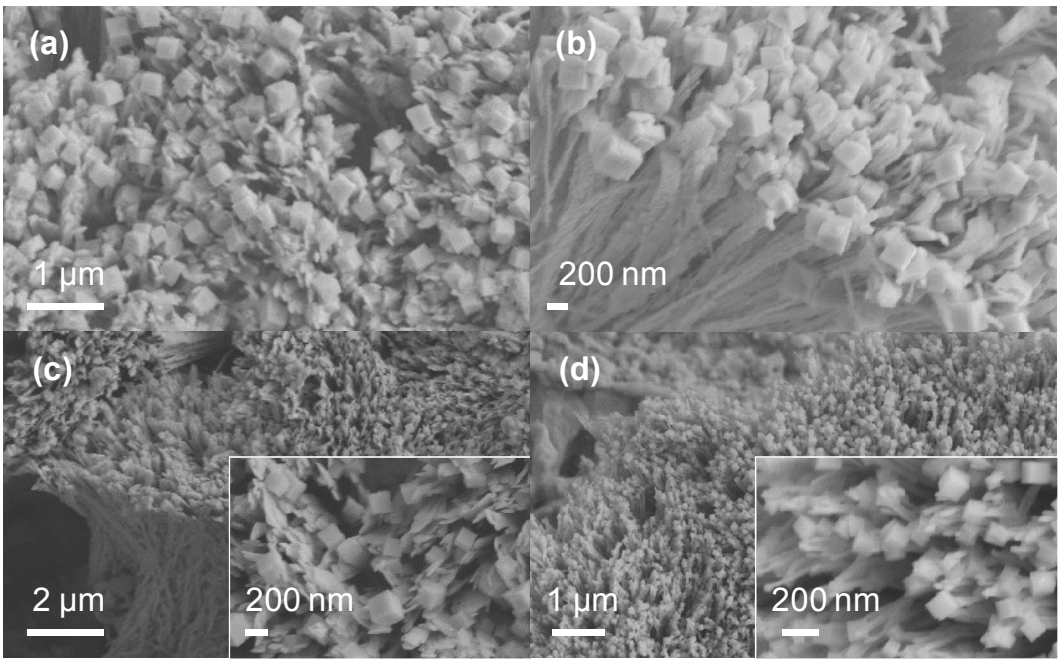

Figure 5. (a) Top-view FESEM image of $Zn_2SnO_4/WO_{2.9}$ heterojunctions for Case 2. (b) High-magnification FESEM image of $Zn_2SnO_4/WO_{2.9}$ for Case 2. (c) Top-view FESEM image of $Zn_2SnO_4/WO_{2.9}$ for Case 3; inset shows the high-magnification FESEM image. (d) Top-view FESEM image of $Zn_2SnO_4/WO_{2.9}$ for Case 4; inset shows the high-magnification FESEM image.

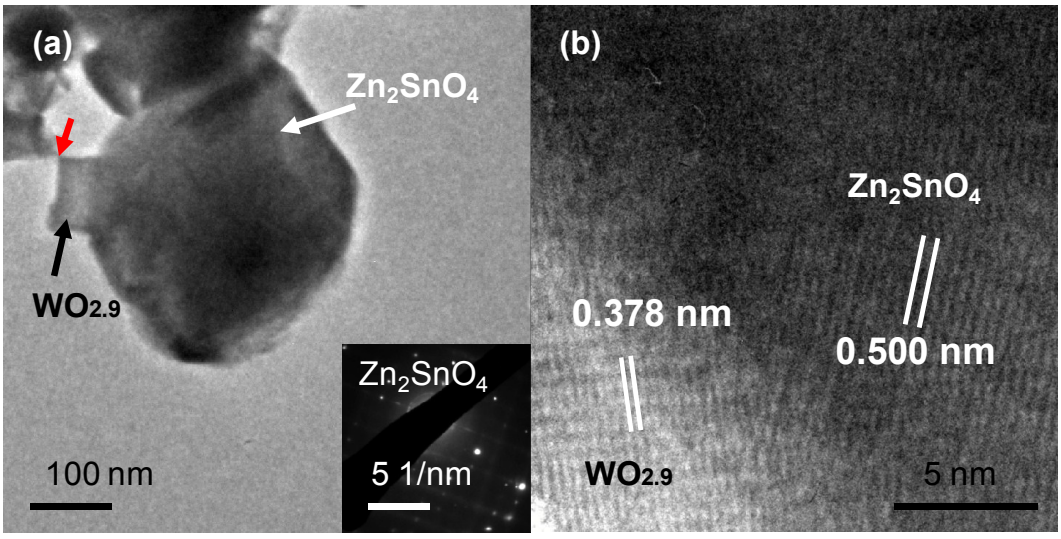

Figure 6. (a) Low-magnification TEM image of a single as-synthesized $Zn_2SnO_4/WO_{2.9}$ heterojunction; inset shows the SAED pattern from Zn_2SnO_4 nanoparticle. (b) HRTEM image of the interface between Zn_2SnO_4 and $WO_{2.9}$.

Zn_2SnO_4 on the Lateral Surfaces of $WO_{2.9}$ Nanowires (Cases 5, 6). In contrast to end-to-end type heterostructure growth, by increasing Sn ion concentration, the as-formed Zn_2SnO_4 nanocubes, obtained from Cases 5 and Case 6, are found not only on the tips of the $WO_{2.9}$ nanowires but also along on the lateral surfaces of the $WO_{2.9}$ nanowires, as shown in **Figure 7**. The growth phenomena observed in Cases 5 and 6 seem to indicate heterogeneous growth of the nanocubes on the nanowires rather than homogenous nucleation in the solution with subsequent deposition on the nanowires. For example, **Figure 7b** evinces a nanocube with a nanowire running through it. Unlike the end-to-end type growth from Cases 1-4, more nucleation sites need to be available on the surface of $WO_{2.9}$ nanowires at the early growth stage to form the hierarchical structure, which may be caused by the increase of "roughness" or grain boundaries[47] of the surface or the increase of the available "kinks" on the surface at the given conditions[65]. From the inset of **Figure 7b**, a considerable amount of nanoparticles with size <10 nm can be found on the surface of $WO_{2.9}$ nanowires, which could serve as active nucleation sites for the subsequent growth of Zn_2SnO_4 nanocubes. In Zhang *et al.*'s work[66], the surfaces of ZnO nanorods were seeded with ZnO nanoparticles (spin-coating) to grow ZnO nanoplates on the nanorod surfaces. Here, the formation of available nucleation sites on the surface of $WO_{2.9}$ nanowires are most likely induced by the increase of Sn:Zn molar ratio, e.g. Sn:Zn=0.1 for Case 2 and Sn:Zn=1.5 for Case 5, and the increase of $SnCl_2$ concentration. During the decomposition of ethylenediamine, the homogeneous nucleation of small Zn_2SnO_4 nanoparticles on the surface of $WO_{2.9}$ nanowires may be triggered by the high saturation level of $SnCl_2$. Moreover, the entire surfaces of $WO_{2.9}$ nanowires can be covered by cubic Zn_2SnO_4 nanocubes with further increasing of $SnCl_2$ concentration (Case 6), as shown in **Figure 7d**. The results seem to confirm the hypothesis for the formation of hierarchical-type $Zn_2SnO_4/WO_{2.9}$ heterojunctions.

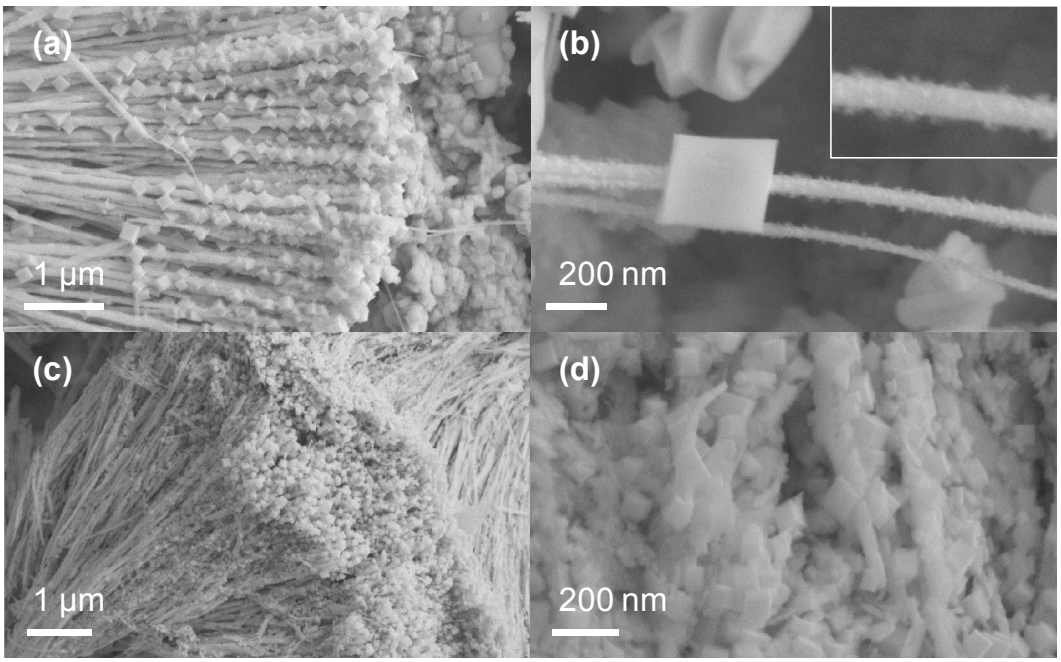

Figure 7. (a) Low-magnification FESEM image of hierarchical $Zn_2SnO_4/WO_{2.9}$ heterojunctions for Case 5. (b) FESEM image shows a cubic Zn_2SnO_4 nanoparticle grown around the $WO_{2.9}$ nanowire from Case 5; inset shows the homogeneous nucleation of nanoparticles with size <10 nm on the surface of $WO_{2.9}$ nanowire. (c) Low-magnification FESEM image of hierarchical $Zn_2SnO_4/WO_{2.9}$ heterojunctions for Case 6. (d) High-magnification FESEM image shows the high yield of cubic Zn_2SnO_4 nanoparticles grown on the surface of $WO_{2.9}$ nanowires.

Coaxial Film of SnO_2 Nanoparticles on $WO_{2.9}$ Nanowires (Cases 7, 8, 9). The concentration of $SnCl_2$ is increased to 5 mM with a Sn:Zn molar ratio of 10 in Case 7; and the solution for Case 8 contains only $SnCl_2$ at 5 mM (following reaction route 5) with the Sn:Zn ratio going to infinity, resulting in the growth of particle-coated-coaxial $SnO_2/WO_{2.9}$ nanowires. The entire surfaces of $WO_{2.9}$ nanowires are covered by layers of SnO_2 nanoparticles, as shown in **Figure 8a** and **8b,** for Cases 7 and 8, respectively. As the Sn:Zn molar ratio increases from 0.25 to 4, the products change from ZnO to Zn_2SnO_4 to SnO_2, as SnO_2 becomes more favorable to precipitate out in the solution at high concentrations of Sn/O-related species[45]. With a much higher Sn:Zn molar ratio

of 10 in Case 7, precipitation of SnO_2 nanoparticles in solution with deposition on the pre-synthesized $WO_{2.9}$ nanowires seems to take place, as seen from **Figure 8c**. From the indexed SAED pattern, inset of **Figure 8c**, the first three highest intensities of 3.35, 2.65, and 1.74 Å, agree well with tetragonal phase SnO_2 (PDF #97-000-9163). The *d*-spacings correspond to reflections from {110}, {101}, and {211} planes of tetragonal SnO_2, respectively. **Figure 8d** shows an HRTEM image from the interface region between $WO_{2.9}$ and SnO_2. The measured diameters of SnO_2 nanoparticles are 6-7 nm. As seen from **Figure 8d**, the measured lattice planes with *d*-spacing of 3.35 Å from the nanoparticles match well with the reflections from {110} planes of SnO_2. Homogeneous nucleation followed by deposition and growth likely results in the uniform coating/adsorption of SnO_2 nanoparticles on the surface of $WO_{2.9}$ nanowires, which is different from the end-to-end type heterogeneous nucleation and growth phenomena for $ZnO/WO_{2.9}$ and $Zn_2SnO_4/WO_{2.9}$ heterojunctions with polyhedron particles at the end of $WO_{2.9}$ nanowires. Usually, the homogeneous nucleation and growth of fine particles need high supersaturation levels of related precursors, which are featured by the sudden formation of a considerable amount of particles in a short time.

To assess the effect of precursor concentration on the nucleation phenomenon and its impact on the resulting heterostructure morphology, another experimental condition (Case 9) is conducted by decreasing both the concentrations of $SnCl_2$ and $C_2H_4(NH_2)_2$ to 0.5 mM, which are 10% of those employed in Case 8. As shown in **Figure 9a** and **9b**, a more film-like coating of SnO_2 on the surfaces of $WO_{2.9}$ nanowires can be discerned, which is different from the more-distinct particle-coating type growths in Cases 7 and 8. With much lower concentration levels of the precursors in the solution, the homogeneous nucleation of abundant SnO_2 nanoparticles with subsequent deposition on the surfaces of $WO_{2.9}$ nanowires become less favorable. Instead, a

layer-by-layer type adsorption and growth process seems to occur, characterized by a more heterogeneous (epitaxial) formation of film-coating of SnO_2 on the $WO_{2.9}$ nanowires. As the synthesis duration is prolonged, the decomposition of $C_2H_4(NH_2)_2$ may continuously build up an increased concentration of OH^-, increasing roughness of the film with ripples/small particles forming on its surface. However, more detailed investigation is still needed to understand the growth phenomenon as functions of precursor concentration and processing duration.

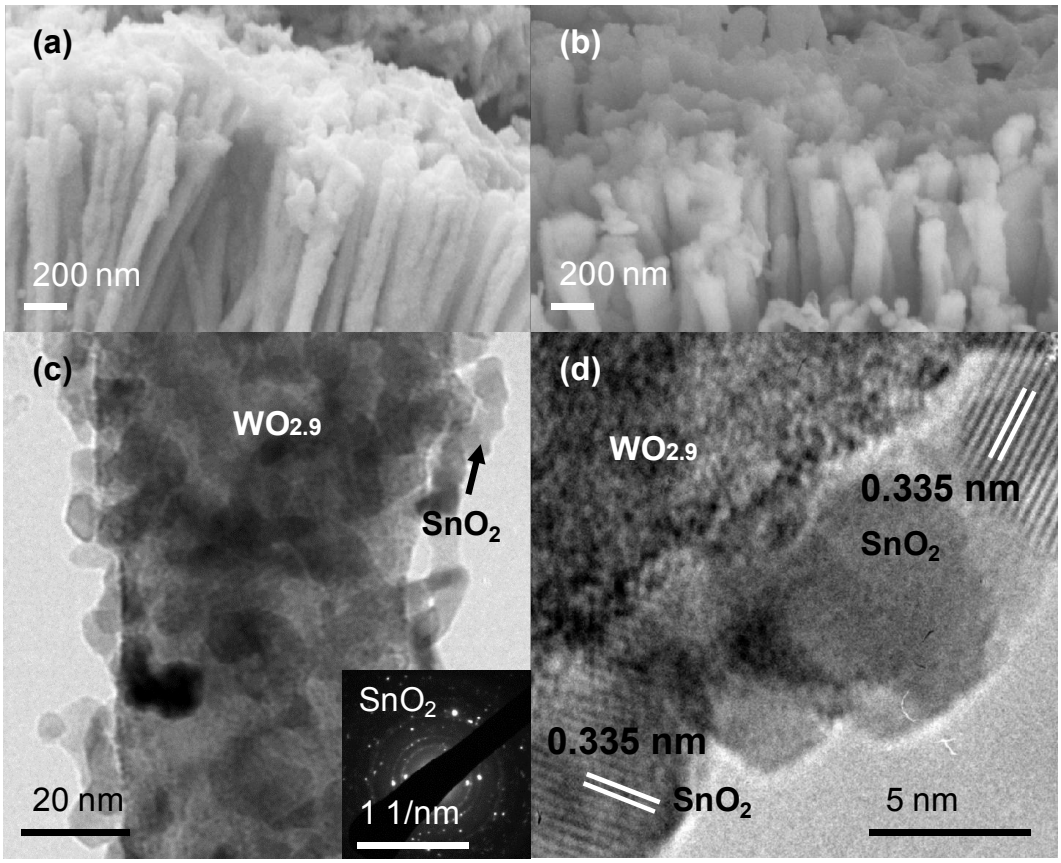

Figure 8. (a) High-magnification FESEM image of $SnO_2/WO_{2.9}$ particle-coating-coaxial nanowires from Case 7. (b) High-magnification FESEM image of $SnO_2/WO_{2.9}$ particle-coating-coaxial nanowires from Case 8. (c) TEM image of a single $SnO_2/WO_{2.9}$ coaxial nanowire; inset shows the SAED pattern from SnO_2. (d) HRTEM image of the interface for $SnO_2/WO_{2.9}$ heterojunction.

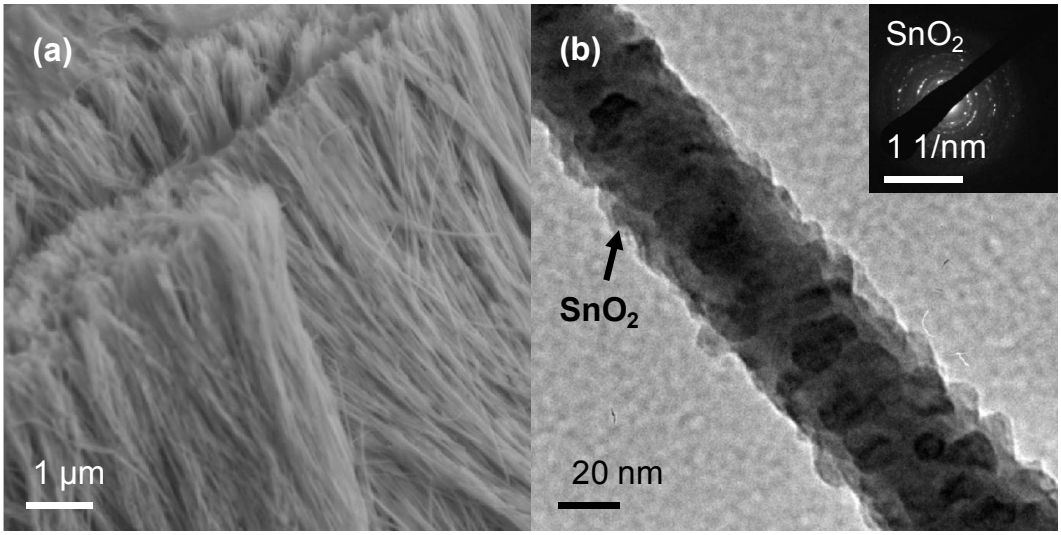

Figure 9. (a) FESEM image of $SnO_2/WO_{2.9}$ film-coating-coaxial nanowires from Case 9. (b) HRTEM image of a single $SnO_2/WO_{2.9}$ coaxial nanowire from Case 9; inset shows the SAED pattern from SnO_2.

Concluding Remarks

In this work, a combined flame and solution syntheses method is used to produce $ZnO/WO_{2.9}$, $Zn_2SnO_4/WO_{2.9}$, and $SnO_2/WO_{2.9}$ nano-heterostructures. Primary flame-synthesized $WO_{2.9}$ nanowires act as the thermodynamically active heterogeneous nucleation or deposition sites for secondary solution-synthesis growth of ZnO nanoplates, Zn_2SnO_4 nanocubes, and SnO_2 nanoparticle films. The end-to-end type formations of $ZnO/WO_{2.9}$ and $Zn_2SnO_4/WO_{2.9}$ heterojunctions are featured by polyhedron nanostructures heterogeneously grown at the tips of $WO_{2.9}$ nanowires. At higher Sn:Zn molar ratios, hierarchical-type formations of $Zn_2SnO_4/WO_{2.9}$ heterojunctions are obtained with Zn_2SnO_4 nanocubes distributed along the lateral surfaces of the $WO_{2.9}$ nanowires. For these cases, the concentrations of $Zn(NO_3)_2$, $SnCl_2$, and $C_2H_8N_2$ are relatively low, with OH^- ions provided slowly by the gradual decomposition of ethylenediamine

($C_2H_8N_2$) at 65 °C. Thus, the low saturations in these cases not only favor heterogeneous formation of nanostructures, but also allow them to have polyhedral crystal faces with good crystallinity. As the Sn:Zn molar ratio goes beyond 10, concentration of Sn-related precursors reach supersatuation, and homogeneous nucleation of nanoparticles occur. The particles are somewhat round though irregular in shape, with polyhedral characteristics. The nanowire surfaces act as favorable deposition sites, resulting in SnO particle-coated coaxial $WO_{2.9}$ nanowires. More film-like heterogeneous growth can be achieved by diluting the precursor concentration. Nanoparticle structures are still seen on the nanowires, indicating that both homogeneous nucleation and heterogeneous growth may be occurring. In this work, the formation of heterostructures with multiple components depends on processing duration, concentrations of different precursors, and presence of pre-synthesized nanowires. For the given solution conditions, well faceted nanocrystals are formed (generally from heterogeneous nucleation), perhaps explaining the good correspondence of the *d*-spacings to the bulk values of the different secondary material compositions. Temperature, precursor concentration, and pH could readily affect structure and morphology, especially for homogeneous nucleation. Although not studied here, the effects of calcination would be interesting. The sequential flame and solution synthesis process presents a promising technique for the fabrication of 1-D-based heterostructured nanomaterials with novel morphologies and interfaces. A study of their physical and chemical properties is currently being conducted.

Methods

In the first step, the burner configuration consists of two converging nozzles with a 19-mm exit diameter and 15-mm separation distance. Airflow as oxidizer is issued from the top burner, and nitrogen-diluted methane flow is issued from the bottom burner, establishing a flat flame in-

between. Co-flowing nitrogen eliminates oxidizer entrainment into the flame, extinguishes the outer flame, and minimizes shear instabilities. For the relative concentrations of fuel and oxidizer used in our experiments, the flame is located on the oxidizer side of the stagnation surface. A tungsten substrate probe (0.5 mm diameter, 99.95% purity) is inserted into the oxidizer side of the flow field (where the gas-phase temperature is 1720 K), and vertically well-aligned arrays of $WO_{2.9}$ nanowires grow from it. In the second step, the substrate (tungsten probe with $WO_{2.9}$ nanowires on its surface) is placed into ethylenediamine ($C_2H_8N_2$) (97%, Fisher Scientific) solutions with different amounts of precursor compositions and concentrations, at 65 °C for 2.5 hours under atmosphere pressure. Zinc nitrate hexahydrate ($Zn(NO_3)_2 \cdot 6H_2O$, 98%, Fisher Scientific) and tin chloride dehydrate ($SnCl_2 \cdot 2H_2O$, 98%, Fisher Scientific) are used as precursors to provide the zinc and tin ions, respectively. For Case 1, the solution contains only zinc nitrate as precursor, which provides the Zn ions to form the desired $ZnO/WO_{2.9}$ heterostructrured nanomaterials. For Cases 2-7, progressively more Sn ions comprise the aqueous solution, affecting the final composition and morphology of the as-produced nanostructures. For Case 8, the solution contains only tin chloride dehydrate as precursor, which provides only Sn ions to form the desired $SnO_2/ WO_{2.9}$ heterostructured nanomaterials. An additional Case 9, using very-low Sn precursor concentration, is examined where a more epitaxial-like SnO_2 coating is formed.

The morphologies of as-produced samples are investigated using field emission scanning electron microscopy (FESEM). Structural features of the samples are investigated using high resolution transmission electron microscopy (HRTEM), and chemical phase is determined using selected area electron diffraction (SAED).

Author information

Corresponding Author

*Email: sdytse@rutgers.edu

Acknowledgements

This work was supported by the Army Research Office (Grant W911NF-08-1-0417) and the National Science Foundation (Grant CBET 0755615). Special thanks are due to Dr. Jafar Al-Sharab for helpful discussions.

Reference

1 A. J. Mieszawska, R. Jalilian, G. U. Sumanasekera and F. P. Zamborini, *Small*, 2007, **3**, 722–756.
2 S. Barth, F. Hernandez-Ramirez, J. D. Holmes and A. Romano-Rodriguez, *Prog. Mater. Sci.*, 2010, **55**, 563–627.
3 Z. Dong, J. F. Al-Sharab, B. H. Kear and S. D. Tse, *Nano Lett.*, 2013, **13**, 4346–4350.
4 D. Li, Y. Wu, R. Fan, P. Yang and A. Majumdar, *Appl. Phys. Lett.*, 2003, **83**, 3186–3188.
5 D.-F. Zhang, L.-D. Sun, C.-J. Jia, Z.-G. Yan, L.-P. You and C.-H. Yan, *J. Am. Chem. Soc.*, 2005, **127**, 13492–13493.
6 M. A. Verheijen, G. Immink, T. de Smet, M. T. Borgström and E. P. A. M. Bakkers, *J. Am. Chem. Soc.*, 2006, **128**, 1353–1359.
7 N. D. Zakharov, P. Werner, G. Gerth, L. Schubert, L. Sokolov and U. Gösele, *J. Cryst. Growth*, 2006, **290**, 6–10.
8 M. S. Gudiksen, L. J. Lauhon, J. Wang, D. C. Smith and C. M. Lieber, *Nature*, 2002, **415**, 617–620.
9 Y. Wu, J. Xiang, C. Yang, W. Lu and C. M. Lieber, *Nature*, 2004, **430**, 61–65.
10 Y. Y. Wu, R. Fan and P. D. Yang, *Nano Lett.*, 2002, **2**, 83–86.
11 A. Lugstein, A. M. Andrews, M. Steinmair, Y.-J. Hyun, E. Bertagnolli, M. Weil, P. Pongratz, M. Schramboeck, T. Roch and G. Strasser, *Nanotechnology*, 2007, **18**, 355306.
12 Z.-Y. Jiang, Z.-X. Xie, X.-H. Zhang, R.-B. Huang and L.-S. Zheng, *Chem. Phys. Lett.*, 2003, **378**, 313–316.
13 F. Xu, X. Liu, S. D. Tse, F. Cosandey and B. H. Kear, *Chem. Phys. Lett.*, 2007, **449**, 175–181.
14 P. M. Rao and X. Zheng, *Nano Lett.*, 2011, **11**, 2390–2395.

15 W. Merchan-Merchan, A. V. Saveliev and W. C. Jimenez, *Proc. Combust. Inst.*, 2011, **33**, 1899–1908.
16 L. Cai, P. M. Rao and X. Zheng, *Nano Lett.*, 2011, **11**, 872–877.
17 F. Xu, X. Liu and S. D. Tse, *Carbon*, 2006, **44**, 570–577.
18 F. Xu, H. Zhao and S. D. Tse, *Proc. Combust. Inst.*, 2007, **31**, 1839–1847.
19 N. K. Memon, F. Xu, G. Sun, S. J. B. Dunham, B. H. Kear and S. D. Tse, *Carbon*, 2013, **63**, 478–486.
20 N. K. Memon, S. D. Tse, J. F. Al-Sharab, H. Yamaguchi, A.-M. B. Goncalves, B. H. Kear, Y. Jaluria, E. Y. Andrei and M. Chhowalla, *Carbon*, 2011, **49**, 5064–5070.
21 N. K. Memon, S. D. Tse, M. Chhowalla and B. H. Kear, *Proc. Combust. Inst.*, 2013, **34**, 2163–2170.
22 N. K. Memon, B. H. Kear and S. D. Tse, *Chem. Phys. Lett.*, 2013, **570**, 90–94.
23 D. J. Milliron, S. M. Hughes, Y. Cui, L. Manna, J. Li, L.-W. Wang and A. P. Alivisatos, *Nature*, 2004, **430**, 190–195.
24 Y. Baek, Y. Song and K. Yong, *Adv. Mater.*, 2006, **18**, 3105–3110.
25 L. Ouyang, K. N. Maher, C. L. Yu, J. McCarty and H. Park, *J. Am. Chem. Soc.*, 2007, **129**, 133–138.
26 X. Gao, T. Gao and L. Zhang, *J. Mater. Chem.*, 2003, **13**, 6–8.
27 H. Kim, Y. Tak, K. Senthil, J. Joo, S. Jeon and K. Yong, *J. Vac. Sci. Technol. B Microelectron. Nanometer Struct.*, 2009, **27**, 2182–2186.
28 H. J. Scheel, in *Liquid Phase Epitaxy of Electronic, Optical and Optoelectronic Materials*, eds. P. Capper and Michaeluk, John Wiley & Sons, Ltd, 2007, pp. 1–19.
29 X. S. Wang, N. Miura and N. Yamazoe, *Sens. Actuators B-Chem.*, 2000, **66**, 74–76.
30 S.-H. Wang, T.-C. Chou and C.-C. Liu, *Sens. Actuators B Chem.*, 2003, **94**, 343–351.
31 I. Jiménez, M. A. Centeno, R. Scotti, F. Morazzoni, A. Cornet and J. R. Morante, *J. Electrochem. Soc.*, 2003, **150**, H72–H80.
32 J. Zhu, S. Wei, M. J. Alexander, T. D. Dang, T. C. Ho and Z. Guo, *Adv. Funct. Mater.*, 2010, **20**, 3076–3084.
33 M. Sadakane, K. Sasaki, H. Kunioku, B. Ohtani, W. Ueda and R. Abe, *Chem. Commun.*, 2008, 6552.
34 S. Sen, P. Kanitkar, A. Sharma, K. P. Muthe, A. Rath, S. K. Deshpande, M. Kaur, R. C. Aiyer, S. K. Gupta and J. V. Yakhmi, *Sens. Actuators B Chem.*, 2010, **147**, 453–460.
35 E. de B. Santos, J. M. de S. e Silva, F. A. Sigoli and I. O. Mazali, *J. Nanoparticle Res.*, 2011, **13**, 5909–5917.
36 S. An, S. Park, H. Ko and C. Lee, *Appl. Phys. A*, 2012, **108**, 53–58.
37 J. Su, L. Guo, N. Bao and C. A. Grimes, *Nano Lett.*, 2011, **11**, 1928–1933.
38 F. Xu, S. D. Tse, J. F. Al-Sharab and B. H. Kear, *Appl. Phys. Lett.*, 2006, **88**, 243115–243115.
39 T. X. Li, H. G. Zhang, F. J. Wang, Z. Chen and K. Saito, *Proc. Combust. Inst.*, 2007, **31**, 1849–1856.
40 N. K. Memon, S. D. Tse, J. F. Al-Sharab, H. Yamaguchi, A.-M. B. Goncalves, B. H. Kear, Y. Jaluria, E. Y. Andrei and M. Chhowalla, *Carbon*, 2011, **49**, 5064–5070.
41 B. Weintraub, Y. Deng and Z. L. Wang, *J. Phys. Chem. C*, 2007, **111**, 10162–10165.
42 D.-F. Zhang, L.-D. Sun, J.-L. Yin and C.-H. Yan, *Adv. Mater.*, 2003, **15**, 1022–1025.
43 J.-M. Jang, J.-Y. Kim and W.-G. Jung, *Thin Solid Films*, 2008, **516**, 8524–8529.

44 N. O. V. Plank, H. J. Snaith, C. Ducati, J. S. Bendall, L. Schmidt-Mende and M. E. Welland, *Nanotechnology*, 2008, **19**, 465603.

45 J. Fang, A. Huang, P. Zhu, N. Xu, J. Xie, J. Chi, S. Feng, R. Xu and M. Wu, *Mater. Res. Bull.*, 2001, **36**, 1391–1397.

46 X. Fu, X. Wang, J. Long, Z. Ding, T. Yan, G. Zhang, Z. Zhang, H. Lin and X. Fu, *J. Solid State Chem.*, 2009, **182**, 517–524.

47 H. T. Ng, J. Li, M. K. Smith, P. Nguyen, A. Cassell, J. Han and M. Meyyappan, *Science*, 2003, **300**, 1249–1249.

48 Z. I. Alferov, *Semiconductors*, 1998, **32**, 1–14.

49 R. S. Wagner and W. C. Ellis, *Appl. Phys. Lett.*, 1964, **4**, 89–90.

50 T. J. Trentler, K. M. Hickman, S. C. Goel, A. M. Viano, P. C. Gibbons and W. E. Buhro, *Science*, 1995, **270**, 1791–1794.

51 B. A. Wacaser, K. A. Dick, J. Johansson, M. T. Borgström, K. Deppert and L. Samuelson, *Adv. Mater.*, 2009, **21**, 153–165.

52 P. Hartman and W. G. Perdok, *Acta Crystallogr.*, 1955, **8**, 525–529.

53 ZHONG Wei-Zhuo, LIU Guang-Zhao, SHI Er-Wei, HUA Su-Kun, TANG Ding-Yuan and DIAO Qiang-Lan, *Sci. China B*, **24**, 349–355.

54 A. Bagabas, A. Alshammari, M. F. Aboud and H. Kosslick, *Nanoscale Res. Lett.*, 2013, **8**, 516.

55 W. J. Li, E. W. Shi, W. Z. Zhong and Z. W. Yin, *J. Cryst. Growth*, 1999, **203**, 186–196.

56 S. G. Kwon, G. Krylova, P. J. Phillips, R. F. Klie, S. Chattopadhyay, T. Shibata, E. E. Bunel, Y. Liu, V. B. Prakapenka, B. Lee and E. V. Shevchenko, *Nat. Mater.*, 2015, **14**, 215–223.

57 G. Shen, D. Chen and C. Zhou, *Chem. Mater.*, 2008, **20**, 3788–3790.

58 W. Merchan-Merchan and M. F. Farahani, *Mater. Sci. Eng. B-Adv. Funct. Solid-State Mater.*, 2013, **178**, 127–134.

59 B. Tan, E. Toman, Y. Li and Y. Wu, *J. Am. Chem. Soc.*, 2007, **129**, 4162–4163.

60 M. Zhang, T. An, X. Hu, C. Wang, G. Sheng and J. Fu, *Appl. Catal. Gen.*, 2004, **260**, 215–222.

61 A. Rong, X. P. Gao, G. R. Li, T. Y. Yan, H. Y. Zhu, J. Q. Qu and D. Y. Song, *J. Phys. Chem. B*, 2006, **110**, 14754–14760.

62 C. Yao, Q. Zeng, G. F. Goya, T. Torres, J. Liu, H. Wu, M. Ge, Y. Zeng, Y. Wang and J. Z. Jiang, *J. Phys. Chem. C*, 2007, **111**, 12274–12278.

63 S. Mathur, M. Veith, M. Haas, H. Shen, N. Lecerf, V. Huch, S. Hüfner, R. Haberkorn, H. P. Beck and M. Jilavi, *J. Am. Ceram. Soc.*, 2001, **84**, 1921–1928.

64 Yu J.H. and Choi G.M., *Sens. Actuators B Chem.*, 2001, **72**, 141–148.

65 B. Li and Y. Wang, *J. Phys. Chem. C*, 2010, **114**, 890–896.

66 C. Zhang, M. Shao, F. Ning, S. Xu, Z. Li, M. Wei, D. G. Evans and X. Duan, *Nano Energy*, 2015, **12**, 231–239.